

Computational fluid dynamics investigation on aortic hemodynamics in double aortic arch before and after ligation surgery

LING, Yunfei, SCHENKEL, Torsten <<http://orcid.org/0000-0001-5560-1872>>, TANG, Jiguo and LIU, Hongtao

Available from Sheffield Hallam University Research Archive (SHURA) at:

<http://shura.shu.ac.uk/30543/>

This document is the author deposited version. You are advised to consult the publisher's version if you wish to cite from it.

Published version

LING, Yunfei, SCHENKEL, Torsten, TANG, Jiguo and LIU, Hongtao (2022). Computational fluid dynamics investigation on aortic hemodynamics in double aortic arch before and after ligation surgery. *Journal of Biomechanics*, 141: 111231.

Copyright and re-use policy

See <http://shura.shu.ac.uk/information.html>

Computational fluid dynamics investigation on aortic hemodynamics in double aortic arch before and after ligation surgery

Yunfei Ling^{a,b}, Torsten Schenkel^c, Jiguo Tang^{b*}, Hongtao Liu^b

^aDepartment of Cardiovascular Surgery, West China Hospital, Sichuan University, Chengdu 610041, China

^bState Key Laboratory of Hydraulics and Mountain River Engineering, College of Water Resource & Hydropower, Sichuan University, Chengdu 610065, China

^cDepartment of Engineering and Mathematics, Sheffield Hallam University, Sheffield S1 1WB, United Kingdom

Abstract: Double aortic arch (DAA) malformation is one of the reasons for symptomatic vascular rings, the hemodynamics of which is still poorly understood. Double aortic arch is the most common type of vascular ring often requiring surgical repair in childhood. The hemodynamics for the DAA remains unclear. This study aims to investigate the blood flow characteristics in patient-specific double aortic arches using computational fluid dynamics (CFD). Seven cases of infantile patients with DAA were collected and their computed tomography images were used to reconstruct 3D computational models. A modified Carreau model was used to consider the non-Newtonian effect of blood and a three-element Windkessel model taking the effect of the age of patients into account was applied to reproduce physiological pressure waveforms. Numerical results show that blood flow distribution and energy loss of DAA depends on relative sizes of the two aortic arches and their angles with the ascending aorta. Ligation of either aortic arch increases the energy loss of blood in the DAA, leading to the increase in cardiac workload. Generally, the rising rate of energy loss before and after the surgery is almost linear with the area ratio between the aortic arch without ligation and the ascending aorta.

Keyword: Double aortic arch; Non-Newtonian fluids; Three-element Windkessel model, Flow distribution; Energy loss

*Corresponding author.
E-mail address: tangjiguo@scu.edu.cn/tangjiguo@sina.cn (J. Tang)

1. Introduction

Double aortic arch (DAA) malformation is the most common cause of symptomatic vascular rings, arising from the persistence of the fourth aortic arches during embryonic development. In general, both left and right arches give rise to ipsilateral separate carotid and subclavian arteries (Hanneman et al., 2017). However, most DAA patients have one arch that is larger in size and extends higher cranially, categorizing the anomaly into dominant right arch (55-70%), dominant left arch (20-35%) and balanced arches (5-10%) (Temur et al., 2021). Symptoms of DAA include wheeze, dyspnea, recurrent pulmonary infection and dysphagia due to tracheal and esophageal compression.

Early surgical repair is recommended for all DAA patients to prevent aggravation of symptoms or even death. In practice, ligating the non-dominant arch with concurrent repair of other anomalies is usually performed on patients with one dominant arch (Alsenaidi et al., 2006; Yang et al., 2019). However, surgeries on balanced arches remain controversial since both arches are similar in diameter and the choice of intervened arch is based predominantly upon surgeons' experience. Subjective judgment may be insufficient considering the complex nature and multiple variations of aortic morphology as well as hemodynamics (Kaldararova et al., 2017), and suboptimal choice of ligated arch may lead to compromised prognosis, including insufficient neurological blood supply and decreased motor function of upper extremities.

Computational fluid dynamics (CFD) can be used to analyze hemodynamics even in complex anatomies (Taylor and Figueroa, 2009; Numata et al. 2016; Zhu et al., 2019; Ling et al., 2021), and has been reported providing highly resolved blood flow metrics for surgeons to base their treatments upon (Pirola et al., 2017; Singh et al., 2016). Although the aortic ligation and aneurysms of patient with single aortic arch were investigated by many researchers, little work on the hemodynamics of DAA with CFD method is published (Miyazaki et al., 2017; Hohri et al., 2021). Furthermore, the above studies are limited to single patients with DAA. In this study, we collected 7

cases of infantile patients with DAA. We performed the numerical simulations with their computed tomography (CT) imaged to investigate the aortic hemodynamics in DAA with different anatomical features. The aim of the present study was to elucidate the aortic hemodynamics in double aortic arch and the changes of flow distribution ratio and energy loss before and after ligating one of aortic arches to provide some references for the surgery.

2. Computational modeling and numerical method

In the present study, the flow is considered to be transient, three-dimensional, and laminar since the mean Reynolds number is less than 1000. The blood is regarded as an incompressible, non-Newtonian fluid with a density of 1060 kg/m³ (Boumpouli et al., 2021). Thus, the conservation equations can be described as:

$$\nabla \cdot \mathbf{v} = 0 \quad (1)$$

$$\rho \frac{\partial \mathbf{v}}{\partial t} + \mathbf{v} \cdot \nabla (\rho \mathbf{v}) = -\nabla P + \nabla \cdot (\mu \nabla \mathbf{v}) \quad (2)$$

where ρ is the blood density, v and P are the blood velocity and pressure. μ is the viscosity and is calculated using a modified Carreau model (Gambaruto et al., 2011; Pereira et al., 2013):

$$\mu = \mu_{\infty} + (\mu_0 - \mu_{\infty}) (1 + (\lambda \dot{\gamma})^2)^{\frac{n-1}{2}} \quad (3)$$

where the zero and infinite strain rate limit viscosities μ_0 and μ_{∞} are equal to 45.6 and 3.2 mPa s, respectively, the relaxation time constant λ is given by 10.03 s and the power law index n is 0.344.

Using constant or scaled inflow boundary conditions often arises in cardiovascular CFD. Effect of the two types of inlet flow rate on the simulation is presented in **Appendix A**. It is found that using constant or scaled inlet flow rate affects the values of WSS and energy loss, but has no obvious effect on the flow distribution ratio of each outlet and the variation trend of energy ratio before and after the surgery. In the present study, the scaled inflow boundary condition is applied. A pulsatile blood flow velocity waveform of ascending aorta (Fig. 1A) obtained by Kocaoglu et al. (2021) is used to reconstruct the inlet flow waves that are not available for the present patients.

75 Considering the difference with different patients, the flow waveform is interpolated to the heart
 76 rate and the average flow rate of each patient. Here, the flow rate is estimated using the weight of
 77 patients, $\bar{Q} = \text{weight} \times 120 \text{ mL/min}$. The heart rate, weight and other patients' information are
 78 given in Table 1. The BSA (body surface area) is estimated based on the references of DuBois and
 79 DuBois (1916) and Wang et al. (1992). Previous works showed that a rigid-wall assumption had no
 80 obvious effect on the resultant flow and stress fields (Pereira et al., 2013; Miyazaki et al., 2017),
 81 thus the arterial wall is assumed to be rigid. A three-element Windkessel model (WK3), as shown in
 82 Fig. 1B, is implemented at each outlet to reproduce physiological pressure P waveforms
 83 (Alimohammadi et al., 2014; Bonfanti et al., 2019):

$$84 \quad P = (R_1 + R_2)Q - R_2C \frac{dp}{dt} + R_1R_2C \frac{dQ}{dt} \quad (4)$$

85 where Q is flow rate, R_1 and R_2 are proximal and distal resistances, and C is the compliance of the
 86 vasculature distal to outlet. The derivative terms can be approximated using the forward Euler
 87 method for cases with small time step Δt :

$$88 \quad P_n = \frac{(R_1 + R_2 + R_1\beta)Q_n - R_1\beta Q_{n-1} + \beta P_{n-1}}{1 + \beta} \quad (5)$$

89 where $\beta = R_2C/\Delta t$. In the present study, we cannot obtain the accurate WK3 model parameters since it
 90 is difficult to measure the patient-specific inlet flow rate and pressure of each outlet for the very
 91 young patients. Therefore, these parameters are determined using the method similar to that used by
 92 Alimohammadi et al. (2014), Qiao et al. (2019) and Liao et al. (2021). Different from these
 93 previous works, the age has a significant effect on the WK3 parameters since the patients are very
 94 young (2-36 months old) in our study. Thus, we consider the effect of age in the following processes
 95 calculating the WK3 parameters. Firstly, the total resistance and the compliance at the i th outlet are
 96 estimated using:

$$97 \quad \bar{P}_i = R_{t,i} \bar{Q}_i \quad (6)$$

$$C_i = \frac{\tau}{R_{t,i}} \quad (7)$$

where the average flow rate \bar{Q}_i is calculated from the 0 Pa boundary condition simulations, the time constant τ is 1.79 s (Simon et al., 1979) and the average outlet pressure \bar{P}_i is estimated based on the standard formula $\bar{P}_i = P_{min} + 1/3(P_{max} - P_{min})$ (Alimohammadi et al., 2014). Since the patients are too young to measure their blood pressure waveform of each outlet, diastolic and systolic blood pressures are utilized to estimate the average outlet pressure of each outlet (Qiao et al., 2020). Then, the proximal resistance R_1 and distal resistance R_2 are calculated using:

$$R_{1,i} = \rho \cdot PWV / A_i \quad (8)$$

$$R_{2,i} = R_{t,i} - R_{1,i} \quad (9)$$

where A_i is the area of the i th outlet, and the pulse wave velocity PWV is related to the patient age and is calculated using the correlation proposed by Jarvis et al. (2020), $PWV=1.3+1.2M$, M is the age of the patient in month. In the present simulations, the coronary artery flow is not considered because the measured inlet flow data is lacked and the consideration of coronary arteries makes the three-element Windkessel model more complex. We thus use the ascending aorta without the coronary arteries as the simulated geometry to reduce the influence of excluding coronary arteries.

The simulations are performed using Ansys Fluent, and user defined functions (UDF) are applied to achieve the modified Carreau viscosity model and the three-element Windkessel model. A velocity table is read into Fluent to achieve the pulsatile velocity of the inlet. A double-precision pressure-based solver is employed. The PISO algorithm is used as the pressure-velocity coupling method. The second-order upwind scheme is adopted for the discretization of the governing equations. The least squared cell- based gradient evaluation method is applied to compute the gradient of the scalar. The standard scheme is used for the pressure interpolation. The time step is set to 0.001 s and the data from the 6th cardiac cycle are used to avoid the start-up effects and to achieve stable results (Cheng et al., 2014; Qiao et al., 2019).

122 The CT images of 7 infantile patients with double aortic arch were collected retrospectively and
 123 used to reconstruct the 3D computational model, as shown in Fig. 1C. The study was approved by
 124 the Ethics Committee of West China Hospital, Sichuan University, Chengdu, China (Ref No. 2022-
 125 26). In addition, written informed consent was obtained from all the guardian on behalf of the child
 126 participant. The diameters of ascending aorta (AA), descending aorta (DA), right carotid artery
 127 (RCA), right subclavian artery (RSA), left carotid artery (LCA), left subclavian artery (LSA) are
 128 summarized in Table 1.

129 The inlet is extruded for over 10 times in their radius to ensure the full development of ejected
 130 flow. The polygonal mesh with 12 prism layers at the walls (growth rate of 1.05) is generated and
 131 used in this work. Numerical simulations for case 1 with meshes of 0.69, 0.91 and 1.10 million cells
 132 are performed to test the mesh independence. The corresponding maximum wall shear stress (WSS)
 133 is 23.251, 23.351 and 23.354 Pa, respectively, resulting in a Grid Convergence Index (GCI) of
 134 0.002% (Celik et al., 2008). Thus, the mesh-generated method for the case with 1.10 million
 135 elements is used for all simulations. All simulations are performed on a server with two 64-core
 136 AMD EPCY-7702 CPUs and 256 G RAM. For each simulation, 60 cores are used and the
 137 computational time is about 30-50 minutes for 100 time steps. The total computational time is about
 138 11-33 hours for the cases with different cardiac cycles.

139 Table 1 Summary of patients' information, sizes of each inlet and outlet and clinical diagnosis

Case	1	2	3	4	5	6	7
Age (months)	9	2	3	11	11	36	36
Sex	Female	Female	Male	Female	Female	Male	Male
Heart rate (bpm)	132	136	160	109	130	162	97
Weight (kg)	9	6	6.8	10.7	8	6	11
Height (cm)	67	60	58	77	72	80	93
Body surface area (m ²)	0.39	0.30	0.31	0.46	0.386	0.37	0.53
AA diameter (mm)	10.14	9.37	9.64	9.25	8.48	7.46	9.21
DA diameter	1.43	5.70	5.37	5.48	6.81	4.85	6.35

(mm)							
RCA diameter	3.18	3.43	3.24	2.84	2.54	2.01	2.89
(mm)							
RSA diameter	4.01	N/A	3.62	3.36	3.08	1.61	2.92
(mm)							
LCA diameter	2.54	3.14	3.18	2.20	3.72	1.84	3.64
(mm)							
LSA diameter	3.62	3.10	3.22	2.41	2.46	2.97	2.83
(mm)							
Angle between	122.1	111.4	120.2	123.0	116.8	97.9	117.8
DAA (°)							
Angle between	39.7	37.8	29.8	27.2	38.7	33.6	41.2
AA and RAA (°)							
Angle between	38.8	54.9	31.3	53.0	28.7	56.7	39.6
AA and LAA (°)							
Clinical	PFO	PFO,	Trachea-	Trachea-	PFO	ASD, trachea- stenosis, pulmonary infection	VSD, MR, PAH
diagnosis		Trachea- stenosis	stenosis	stenosis			

140 PFO, patent foramen ovale; VSD, ventricular septal defect; MR, mitral regurgitation; PAH, pulmonary arterial
141 hypertension; ASD, atrial septal defect.

142
143 In the present study, flow distribution ratio (FDR), energy loss (EL), spatial averaged WSS
144 (SAWSS) and time averaged WSS (TAWSS) are calculated and analyzed. The FDR is defined as
145 the flow rate ratio of each carotid artery and subclavian artery to ascending aorta:

$$146 \quad FDR = \frac{Q_{out,i}}{Q_{in}} \times 100\% \quad (10)$$

147 EL is calculated by the drops of static pressure and dynamic pressure between the inlet and the
148 outlets:

$$149 \quad EL = (P_{in} + \frac{1}{2} \rho \bar{u}_{in}^2) Q_{in} - \sum_{outlet} (P_{out} + \frac{1}{2} \rho \bar{u}_{out}^2) Q_{out} \quad (11)$$

150 where \bar{u}^2 is the average blood velocity.

151 SAWSS and TAWSS are obtained by averaging the WSS on the wall of the whole vessel at
152 different time and the local WSS through a cardiac cycle, respectively, and can be expressed as:

153
$$SAWSS = \frac{1}{S} \int_S |\tau(s, t)| ds \quad (12)$$

154
$$TAWSS = \frac{1}{T} \int_0^T |\tau(s, t)| dt \quad (13)$$

155 where S and T are the area of surface wall and the cardiac period.

156 3. Results and discussion

157 3.1. Hemodynamics of DAA before and after removing aortic arch

158 For the patient with DAA, it is necessary to determine which aortic arch should be ligated
159 before the surgery. However, this is very difficult due to the complex hemodynamics of DAA,
160 especially for the patient with balanced arches (Hohri et al., 2021). To better guide the surgeries,
161 here we discuss the hemodynamics of DAA before and after ligating right aortic arch (RAA) and
162 left aortic arch (LAA) using a typical balanced geometry model (case 1). Fig. 2 shows the
163 distribution of averaged wall pressure and the blood flow velocity streamlines during peak systole
164 before and after the surgery. The wall pressure of the arteries gradually decreases from ascending
165 aorta to descending aorta along the blood flow direction. The high-pressure region occurs at the
166 bifurcation of the two aortic arches due to the collision of blood upon the vessel wall directly, which
167 will not be observed in single aortic arch. Ligating either aortic arch has no obvious effect on the
168 maximum wall pressure of the arteries, as shown in Fig. 2. The wall pressure distribution is not
169 changed obviously after the ligation of LAA or RAA. As for the streamlines, velocity magnitude is
170 high in the RCA, RSA, LCA and LSA, as expected. After the ligation of one aortic arch, the
171 maximum velocity increases obviously, and the streamlines get more helical in the carotid and
172 subclavian arteries in the ligated side of ascending aorta.

173 Fig. 3 shows the variations of blood flow rate and pressure at each outlet during a cardiac cycle

for case 1. The results of other cases are provided in **Appendix B**. The time-averaged flow rates from each outlet are summarized in **Appendix C**. The outlet blood flow and pressure show a similar trend before and after the ligation either aortic arch. Over 44% of blood outflows through the descending aorta in the original DAA case, and this ratio decreases after the surgery slightly. The flow rate peak of RCA, RSA, LCA and LSA occurs earlier than the inlet flow peak, but that of descending aorta is slightly later than the inlet flow peak. The pressure of descending aorta is reduced when one of aortic arches is ligated, but that of RCA, RSA, LCA and LSA is increased after the surgery.

The variation of SAWSS and the distribution of TAWSS are shown in Fig. 4. Although the temporal variation of SAWSS exhibits a similar shape, its maximum is increased after ligating one of the aortic arches because of the increase in flow rate in the remaining untreated aortic arch. It is worth noting that TAWSS is elevated considerably in the bifurcation between two aortic arches after ligating RAA owing to the larger angle between AA and LAA than that between AA and RAA. When the RAA is ligated, more blood flows through the LAA with an obvious change in flow direction, leading to a high-velocity gradient region.

Fig. 5 shows the energy loss for DAA in case 1 without surgery, ligating LAA or RAA. Similar to the results of an adult single aortic arch (Qiao et al., 2019), the EL for DAA reaches its maximum ($t/T=0.18$) before peak systole ($t/T=0.23$). After the ligation of either aortic arch, the EL reaches the maximum at $t/T=0.114$. The time averaged EL is 6.1 mW before the surgery, while it increases to 9.5 mW (+55%) and 8.5 mW (+39%) after the ligation of LAA and RAA, respectively. This indicates that ligating one of the aortic arches for the patient with DAA will increase the cardiac workload. Although the diameters of LAA and RAA are very similar in case 1, the difference of EL after the removal of LAA and RAA can reach 1 mW, or 16% higher EL for the unfavorable variant. It has to be noted that case 1 is the case that shows the smallest changes before/after and between left and right AA ligations, other cases show more dramatic differences.

3.2. Effect of anatomical features on operative effect

Fig. 6 shows the effect of anatomical features on the blood flow distribution from each outlet and the ratio of blood flow going to brain (LCA and RCA) and to systemic vessels (LSA, RSA and DA) before and after the surgery. Table 2 summarizes the diameter of RAA and LAA, and the FDR of LAA (LCA and LSA) and RAA (RCA and RSA). About 20%-40% blood outflows through LCA and RCA to the brain of patients, as shown in Fig. 6B. For the size-balanced DAA case 5, the FDR of RAA and LAA is similar. However, for the size-balanced DAA cases 1 and 2, the FDR of RAA and LAA differs from each other obviously, similar to the results of an adult patient with DAA reported by Hohri et al. (2021). For the unbalanced DAA cases 3 and 4, the larger aortic arch has higher flow rate, but the FDR of RAA and LAA is not different considerably for the cases 6 and 7, as shown in Fig. 6A. It is more reasonable for determining the dominant arch using the blood flow rate from the left and right carotid and subclavian arteries rather than the diameter of RAA and LAA based on the study of Hohri et al. (2021). Thus, determining the dominant arch of DAA with the CFD method may be more valid than that only with the CT images owing to the considerable effect of various anatomical features.

Table 2 Summary of diameter and FDR of RAA and LAA

Case	1	2	3	4	5	6	7
LAA diameter (mm)	7.24	6.24	6.12	5.10	5.87	3.09	6.60
RAA diameter (mm)	7.37	6.57	8.18	7.73	6.17	6.80	5.03
FDR of LAA (LCA and LSA) (%)	20.38	29.21	21.89	15.81	28.66	20.74	28.99
FDR of RAA (RCA and RSA) (%)	34.65	17.85	36.64	35.21	24.72	24.56	26.88

It is noted that, for the size-balanced cases 1, 2 and 5 and the slightly unbalanced cases 3 and 7 (area ratio of arches less than 2), there is no obvious change in the blood flow distribution before and after either aortic arch. However, for the severely unbalanced cases 4 and 6 (area ratio of arches larger than 2), the blood flowing out from the descending aorta is disturbed after the ligation of RAA (larger arch) obviously, leading to the decrease in the FDR of DA. However, this effect is not

noticeable after ligating the LAA (smaller arch). This is due to that the blood out from descending aorta has to flow through an aortic arch with larger flow resistance after the surgery, resulting in the reduction of FDR of descending aorta. The above simulation results implicate that arch area ratio of 2 may be the critical value determining whether the smaller arch must be the ligated one in the surgery.

The energy loss throughout a cardiac cycle for different patients before and after surgeries is shown in Fig. 7. It can be seen that the energy loss for case 6 is considerably larger than other cases due to the poorly developed aortic arch. After ligating either aortic arch, the energy loss will increase slightly for most cases, as shown in Fig. 7A. While in size-balanced cases (case 1) we observe only minor differences (16%) between RAA and LAA ligation, in unbalanced cases this difference can be as high as 264% (Case 6, LAA vs RAA ligation). This total energy loss is concurrent with a drop in descending aorta FDR. Our results show that in all the cases studied the blood supply to the subclavian and carotid arteries is unimpeded or slightly increased in most cases, and increased even in the critical cases (Case 6, RAA ligation), while support to the lower body is most directly affected negatively in the critical cases. In order to support surgeons in their decision making, we propose two geometric parameters to show the effect of anatomical features of DAA on the energy loss after the surgery. The first one is the area ratio of the ascending aorta to the aortic arch without ligation A_0/A_{rem} . The other one is the angle between the normal direction of ascending aorta and the aortic arch without ligation θ_{rem} , as shown in Fig. 7B. Figure 7 C and D shows the dependency of EL on the area ratio A_0/A_{rem} in panel C and on the angle θ_{rem} in panel D. The dependency of the respective other parameter – angle in panel C, and area ratio in panel D – is shown in the marker size. A statistical analysis of the data is also performed and the results are given in **Appendix D**. The coefficient of determination R^2 that is a statistical measure in a regression model is used to describe the independent of energy loss ratio on different variables. It is interesting that the energy loss ratio before and after the surgery depends on the A_0/A_{rem} ($R^2=0.805$)

246 whichever aortic arch is ligated, as shown in Fig. 7 C. While in the current sample the largest EL
 247 increases were seen for RAA ligations – consistent with the higher occurrence of RAA dominant
 248 cases – the correlation between EL increase and area ratio is clear and linear in Fig. 7 C. Although
 249 both EL_{before} and EL_{after} are affected by the θ_{rem} due to the change of flow direction in the DAA, the
 250 correlation between EL ratio and θ_{rem} is less clear ($R^2=0.424$) in Fig. 7 D. While there is a
 251 correlation between angle and EL there are more outliers in this graph. It is interesting, though, that
 252 these outliers are all RAA dominant cases, where the RAA ligation leads to a relatively low EL for a
 253 high angle case (case 2) and to relatively low EL for low angle cases (cases 3 and 5). Thus, based
 254 on the simulation results, the variation of FDR and energy loss after the surgery of DAA can be
 255 estimated by A_R/A_L , θ_R/θ_L and A_0/A_{rem} roughly to help to optimize the surgical planning.

256 3.3. Limitations

257 In this study, we perform simulations with a series of patient-specific geometries reconstructed
 258 from CT images taking the Non-Newtonian effect into account. However, the inlet and outlet
 259 conditions are still unsure since the patients are too young (2-36 months old) to measure their blood
 260 flow velocity in the present study. To overcome this issue, an inlet velocity waveform measured by
 261 Kocaoglu et al. (2021) not the patient-specific one is used and reconstructed based on the patient-
 262 specific heart rate and the average flow rate estimated using the weight of patients, and the three-
 263 element Windkessel model is applied to reproduce physiological pressure waveforms of each outlet.
 264 In addition to this, similar to most of previous studies, the vessel wall is assumed to be rigid and a
 265 flat velocity profile is given to the extruded boundary. Some previous works showed that the above
 266 assumptions have no obvious effect on blood flow ratio and the distal blood flow of the aortic arch
 267 but affect the value of WSS (Miyazaki et al., 2017; Boumpouli et al., 2021).

268 4. Conclusions

269 The present study investigated the patient-specific blood flow in the double aortic arch (DAA)
 270 before and after surgery with the CFD method. We collected seven cases of infantile patients with

271 DAA and used their computed tomography images to reconstruct 3D computational models. A
272 three-element Windkessel model taking the effect of patient age into account was applied to
273 reproduce physiological pressure waveforms in the simulations. Results show that the anatomical
274 features and surgery program have a considerable effect on the WSS, flow distribution ratio and
275 energy loss for DAA. After ligating one of the aortic arches, the blood flow from the descending
276 aorta is generally reduced when the area ratio of the arch area ratio is larger than 2. The energy loss
277 ratio before and after ligating one aortic arch is proportional to the area ratio of the remained aortic
278 arch in surgery to the ascending aorta. Overall, the present study indicates that the CFD analysis can
279 contribute to a further understanding of hemodynamics in DAA and provide some references for the
280 surgery.

281 **CRedit authorship contribution statement**

282 **Yunfei Ling:** Conceptualization, Investigation, Writing - original draft, Funding acquisition.
283 **Torsten Schenkel:** Formal analysis, Data Curation, Writing - original draft, Writing - review &
284 editing, Visualization. **Jiguo Tang:** Conceptualization, Supervision, Methodology, Writing - original
285 draft, Writing - review & editing, Project administration, Funding acquisition. **Hongtao Liu:**
286 Validation, Software, Formal analysis.

287 **Declaration of Competing Interest**

288 The authors declare that they have no known competing financial interests or personal
289 relationships that could have appeared to influence the work reported in this paper.

290 **Acknowledgements**

291 The authors are profoundly grateful to the financial supports of the Sichuan Science and
292 Technology Program (Grant No. 2021YJ0374) and the 1·3·5 project for disciplines of excellence-
293 Clinical Research Incubation Project, West China Hospital, Sichuan University (ZYJC21064).

294 **References**

295 Alsenaidi, K., Gurofsky, R., Karamlou, T., Williams, W.G., McCrindle, B.W., 2006. Management

296 and outcomes of double aortic arch in 81 patients. *Pediatrics* 118, 1336-1341.

297 Alimohammadi, M., Agu, O., Balabani, S., Díaz-Zuccarini, V., 2014. Development of a patient-
 298 specific simulation tool to analyse aortic ligations: Assessment of mixed patient-specific flow
 299 and pressure boundary conditions. *Med. Eng. Phy.* 36, 275-284.

300 Bonfanti, M., Franzetti, G., Maritati, G., Homer-Vanniasinkam, S., Balabani, S., Díaz-Zuccarini, V.,
 301 2019. Patient-specific haemodynamic simulations of complex aortic ligations informed by
 302 commonly available clinical datasets. *Med. Eng. Phys.* 71, 45-55.

303 Boumpouli, M., Sauvage, E.L., Capelli, C., Schievano, S., Kazakidi, A., 2021. Characterization of
 304 flow dynamics in the pulmonary bifurcation of patients with repaired tetralogy of fallot: A
 305 computational approach. *Front. Cardiovasc. Med.* 8, 703717.

306 Celik, I., Ghia, U., Roache, P. J., Freitas, C. J., Coleman, H., Raad, P. E., 2008. Procedure for
 307 estimation and reporting of uncertainty due to discretization in CFD applications. *J. Fluid. Eng.*,
 308 130, 078001.

309 Cheng, Z., Juli, C., Wood, N. B., Gibbs, R. G. J., Xu, X. Y., 2014. Predicting flow in aortic ligation:
 310 comparison of computational model with PC-MRI velocity measurements. *Medical Engineering*
 311 *and Physics* 36, 1176-1184.

312 DuBois D., DuBois E.F., 1916. A formula to estimate the approximate surface area if height and
 313 weight be known. *Arch. Intern. Medicine* 17 863-71.

314 Gambaruto, A.M., Janela, J., Moura, A., Sequeira, A., 2011. Sensitivity of hemodynamics in a
 315 patient specific cerebral aneurysm to vascular geometry and blood rheology. *Math. Biosci. Eng.*
 316 8, 409–423.

317 Hanneman, K., Newman, B., Chan, F., 2017. Congenital Variants and Anomalies of the Aortic Arch.
 318 *Radiographics* 37, 32-51.

319 Hohri, Y., Numata, S., Itatani, K., Inoue, T., Yaku, H., 2021. Determination of the dominant arch by
 320 computational fluid dynamics analysis using computed tomography images in double aortic

321 arch. *Int. J. Cardiovasc. Imaging* 37, 2573-2575.

322 Jarvis K., Soulat G., Scott M., Vali A., Pathrose A., Syed A.A., Kinno M., Prabhakaran S., Collins
323 J.D., Markl M., Investigation of aortic wall thickness, stiffness and flow reversal in patients with
324 cryptogenic stroke: a 4D flow MRI study, *J. Magn. Reson. Imag.* 53, 942-952.

325 Kaldararova, M., Simkova, I., Varga, I., Tittel, P., Kardos, M., Ondriska, M., Vrsanska, V., Masura,
326 J., 2017. Double aortic arch anomalies in Children: A Systematic 20-Year Single Center Study.
327 *Clin. Anat.* 30, 929-939.

328 Kocaoglu, M., Pednekar, A., Tkach, J. A., Taylor, M.D., 2021. Quantitative assessment of velocity
329 and flow using compressed SENSE in children and young adults with adequate acquired
330 temporal resolution. *J. Cardiovasc. Magn. Reson.* 23, 113.

331 Liao, Z.J., Qin, S.L., Chen, R.L., Cai, X.C., 2021. A parallel domain decomposition method for
332 large eddy simulation of blood flow in human artery with resistive boundary condition. *Comput.*
333 *Fluids* 232, 105201.

334 Ling, Y.F., Tang, J.G., Liu, H., 2021. Numerical investigation of two-phase non-Newtonian blood
335 flow in bifurcate pulmonary arteries with a flow resistant using Eulerian multiphase model.
336 *Chem. Eng. Sci.*, 233, 116426.

337 Miyazaki, S., Itatani, K., Furusawa, T., Nishino, T., Sugiyama, M., Takehara, Y., Yasukochi, S,
338 2017. Validation of numerical simulation methods in aortic arch using 4D Flow MRI. *Heart*
339 *Vessels* 32, 1032-1044.

340 Numata, S., Itatani, K., Kanda, K., Doi, K., Yamazaki, S., Morimoto, K., Manabe K., Ikemoto, K.,
341 Yaku, H., 2016. Blood flow analysis of the aortic arch using computational fluid dynamics.
342 *European Journal of Cardio-Thoracic Surgery*, 49, 1578-1585.

343 Pereira, J. M. C., Serra e Moura, J. P., Ervilha, A. R., Pereira, J. C. F., 2013. On the uncertainty
344 quantification of blood flow viscosity models. *Chem. Eng. Sci.* 101, 253-265.

345 Pirola, S., Cheng, Z., Jarral, O.A., O'Regan, D.P., Pepper, J.R., Athanasiou, T., Xu, X.Y., 2017. On

the choice of outlet boundary conditions for patient-specific analysis of aortic flow using computational fluid dynamics. *J. Biomech.* 60, 15-21.

Qiao, Y., Fan, J., Ding, Y., Luo, K., Zhu, T., 2019. A primary computational fluid dynamics study of pre-and post-TEVAR with intentional left subclavian artery coverage in a type B aortic ligation. *J. Biomech. Eng.* 141, 111002.

Qiao, Y., Mao, L., Ding, Y., Fan, J., Zhu, T., Luo, K., 2020. Hemodynamic consequences of TEVAR with in situ double fenestrations of left carotid artery and left subclavian artery. *Med. Eng. Phy.* 76, 32-39.

Simon, A.C., Safar, M., Levenson, J., London, G., Levy, B., Chau, N., 1979. An evaluation of large arteries compliance in man. *Am. J. Physiol.-Heart C.* 237, H550-H554.

Singh, S.D., Xu, X.Y., Wood, N.B., Pepper, J.R., Izgi, C., Treasure, T., Mohiaddin, R.H., 2016. Aortic flow patterns before and after personalised external aortic root support implantation in Marfan patients. *J. Biomech.* 49, 100-111.

Taylor, C. A., Figueroa, C. A., 2009. Patient-specific modeling of cardiovascular mechanics. *Annual Review of Biomedical Engineering*, 11, 109-134.

Temur, H.O., Yozgat, C.Y., Uzuner, S., Ugurlucan, M., Yazan, H., Cakir, E., Yozgat, Y., 2021. Balanced Double Aortic Arch Causing Persistent Respiratory Symptoms Mimicking Asthma in an Infant. *J. Pediatr. Intensive. Care* 10, 162-166.

Wang Y., Moss J., Thisted R., 1992. Predictors of body surface area. *J. Clin. Anesth.* 4, 4-10.

Yang, Y., Jin, X., Pan, Z., Li, Y., Wu, C., 2019. Diagnosis and surgical repair of congenital double aortic arch in infants. *J. Cardiothorac. Surg.* 14, 160.

Zhu, Y., Zhan, W., Hamady, M., Xu, X.Y., 2019. A pilot study of aortic hemodynamics before and after thoracic endovascular repair with a double-branched endograft. *Medicine in Novel Technology and Devices* 4, 100027.

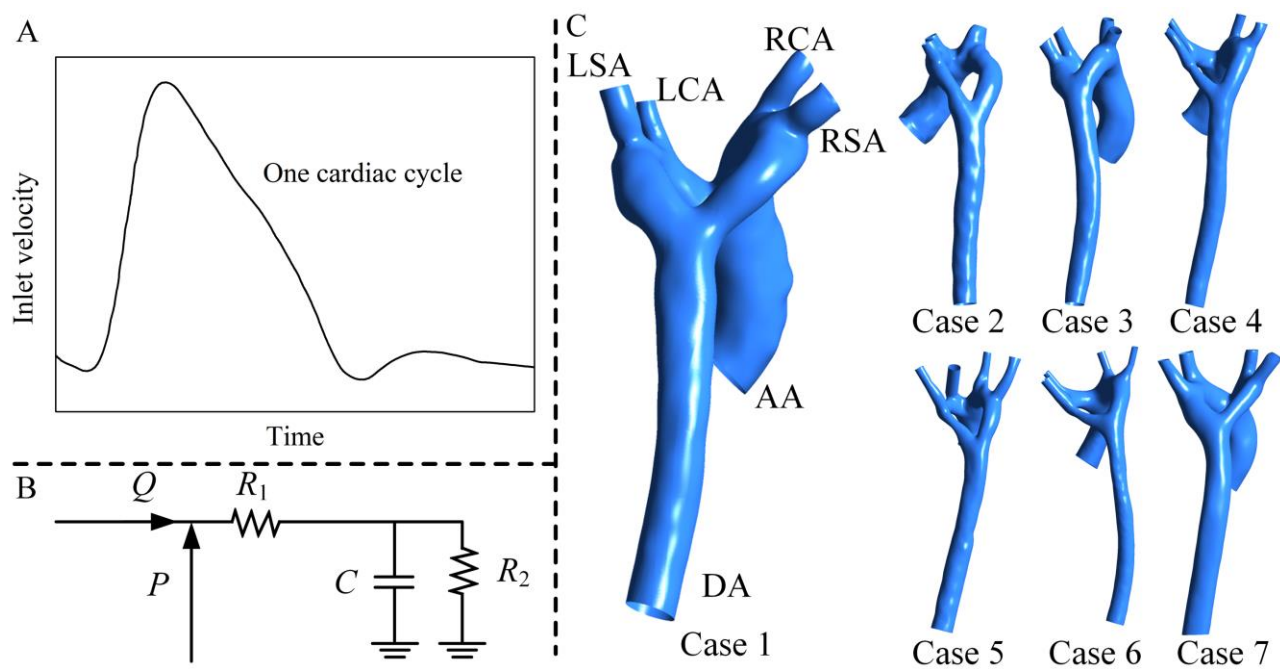


Fig. 1 (A) mass flow rate of inlet from reference of Kocaoglu et al. (2021), (B) three element Windkessel model coupled at each outlet, (C) geometries from different patients.

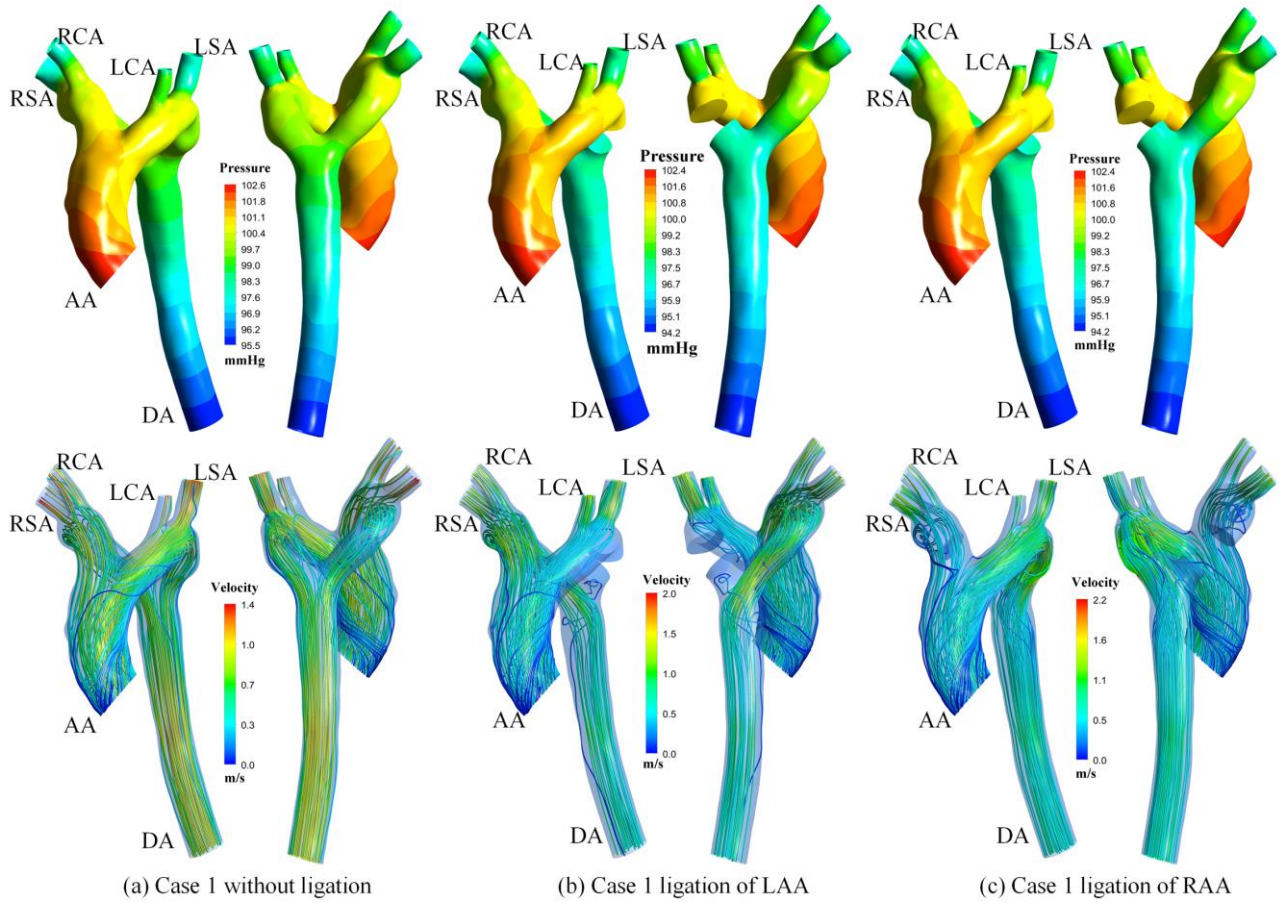


Fig. 2 Distribution of average wall pressure and blood flow velocity streamlines during peak systole: (a) DAA, (b) LAA ligation, (c) RAA ligation.

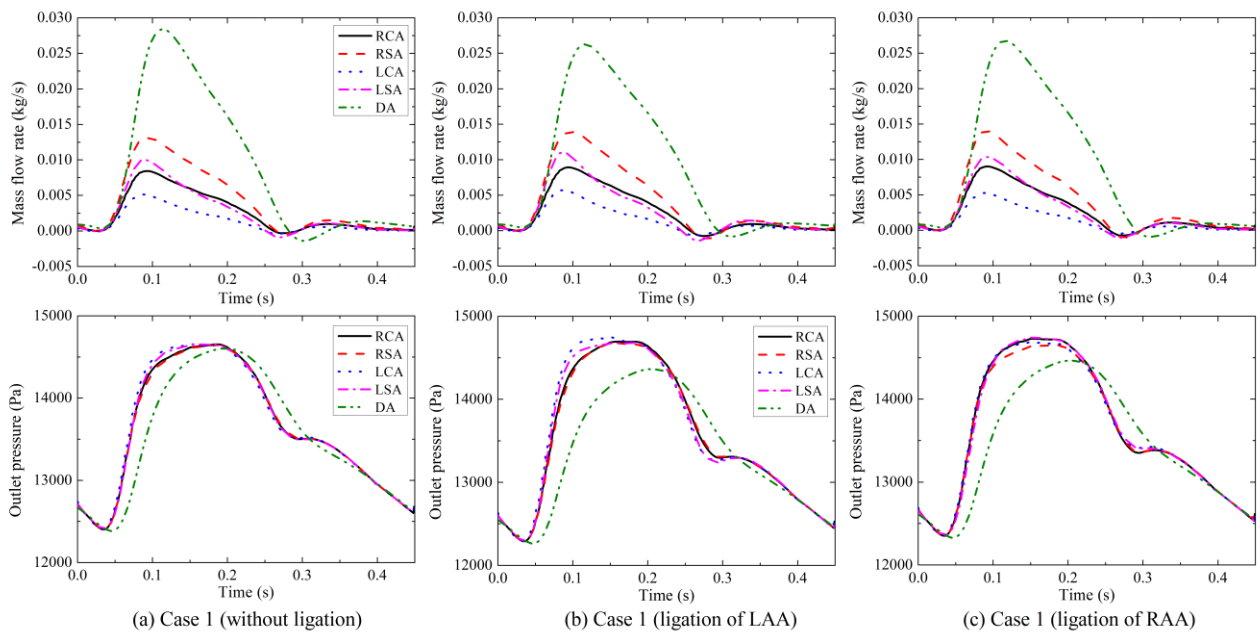


Fig. 3 Variation of blood flow and pressure rate at each outlet during a cardiac cycle.

9

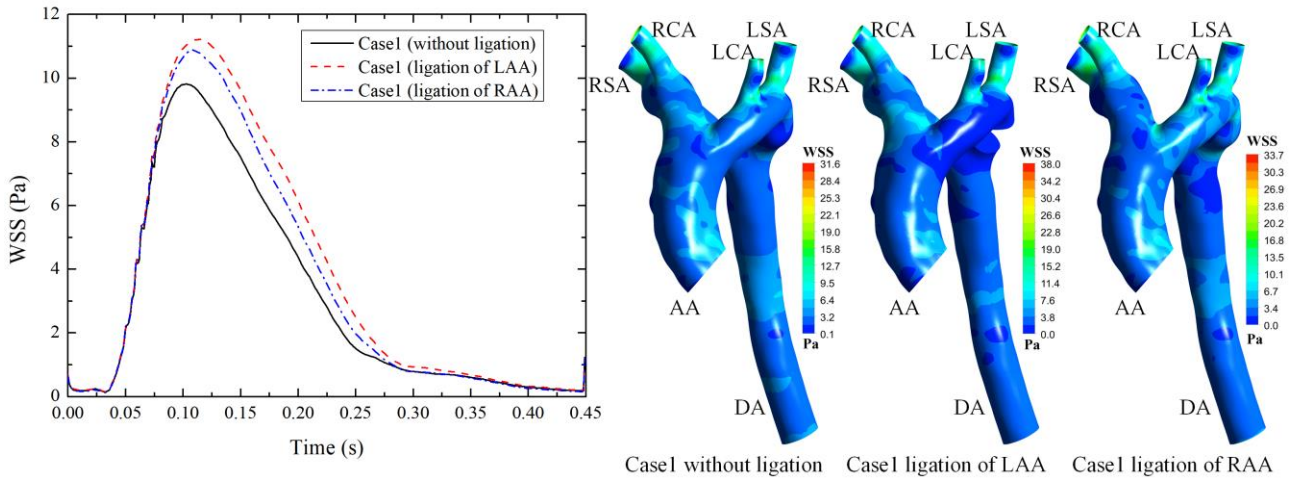


Fig. 4 Variation of SAWSS during a cardiac cycle and distribution of TAWSS.

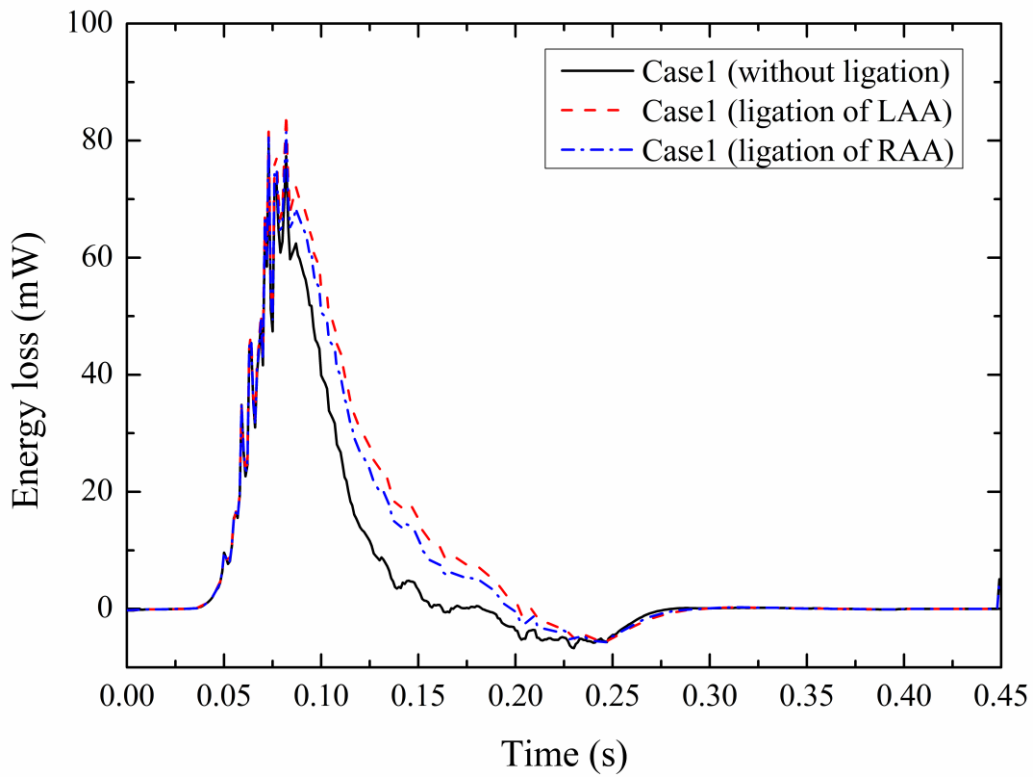


Fig. 5 Variation of energy loss during a cardiac cycle, the time averaged EL is 6.1 mW, 9.5 mW and 8.5 mW before the surgery and after ligating LAA and RAA, respectively.

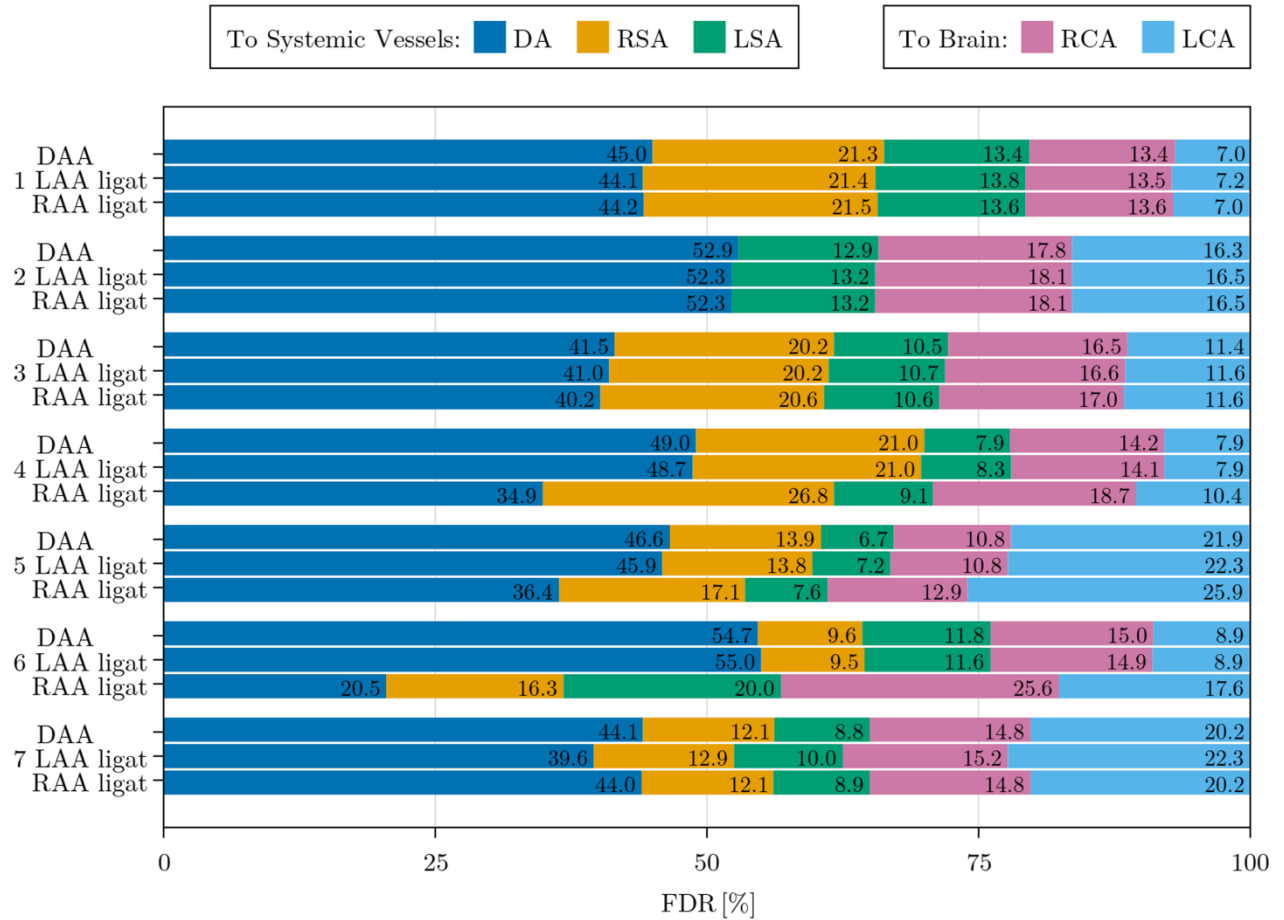


Fig. 6 Variation of Flow Distribution Ratio before (DAA) and after ligation of either aortic arch (LAA diss, RAA diss): (A) FDR of each outlet, (B) FDR going to brain (LCA and RCA) and to systemic vessels (LSA, RSA and DA). Note: case 2 has no subclavian branching from the right aortic arch (RSA).

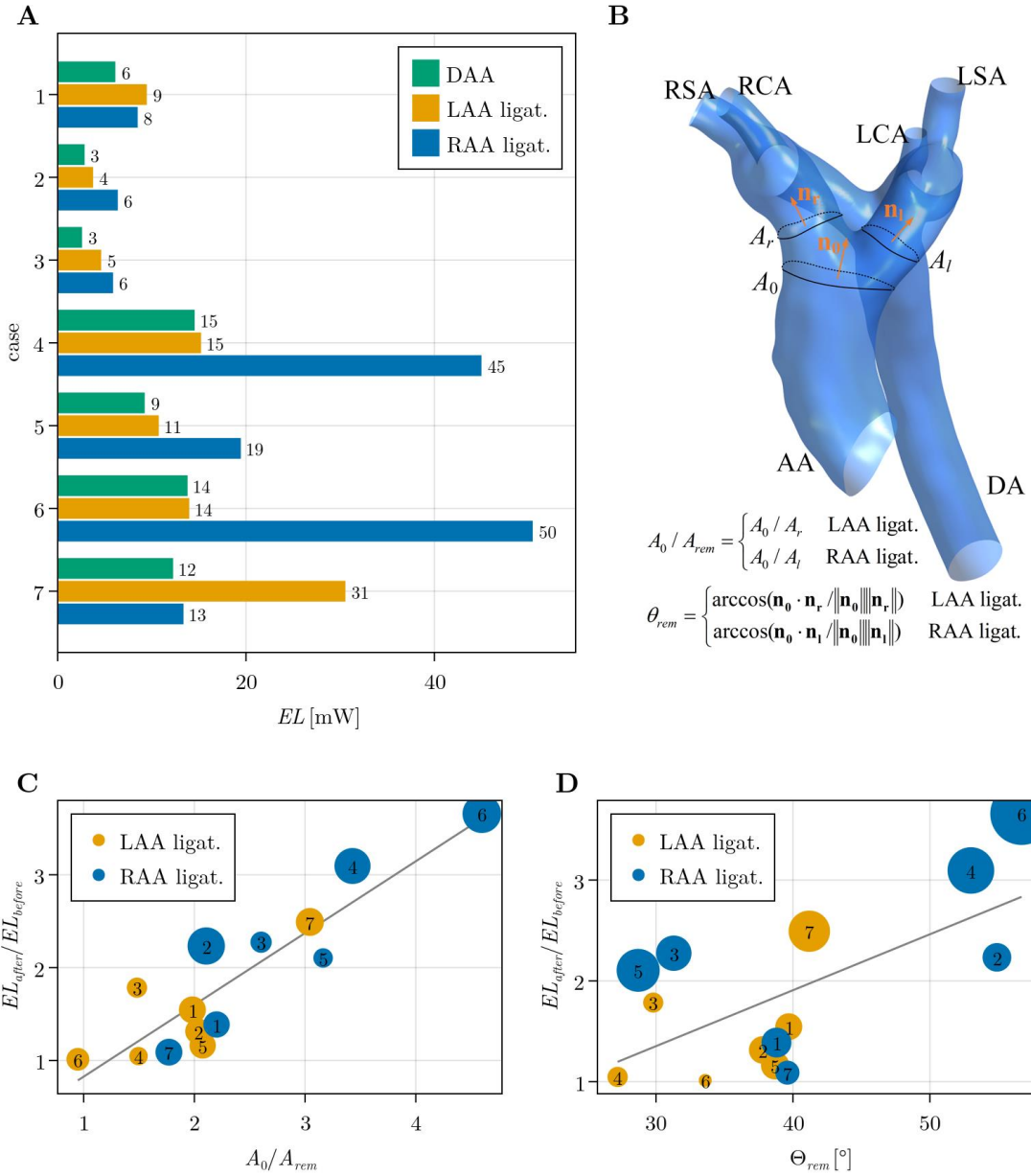


Fig. 7 Energy losses in double aortic arch (DAA) and for dissected LAA and RAA: (A) time averaged energy loss, (B) Definition of area ratio of the ascending aorta to the aortic arch without ligation and angle between the normal direction of ascending aorta and the aortic arch without ligation, (C) and (D) relative EL change after ligation of LAA or RAA dependent on: (C) area ratio total over remaining cross sectional area, (D) angle between ascending aorta and remaining branch (marker size shows (C) angle θ_{rem} , (D) area ratio; marker label shows case number).

1 Table 1 Summary of patients’ information, sizes of each inlet and outlet and clinical diagnosis

Case	1	2	3	4	5	6	7
Age (months)	9	2	3	11	11	36	36
Sex	Female	Female	Male	Female	Female	Male	Male
Heart rate (bpm)	132	136	160	109	130	162	97
Weight (kg)	9	6	6.8	10.7	8	6	11
Height (cm)	67	60	58	77	72	80	93
Body surface area (m²)	0.39	0.30	0.31	0.46	0.386	0.37	0.53
AA diameter (mm)	10.14	9.37	9.64	9.25	8.48	7.46	9.21
DA diameter (mm)	1.43	5.70	5.37	5.48	6.81	4.85	6.35
RCA diameter (mm)	3.18	3.43	3.24	2.84	2.54	2.01	2.89
RSA diameter (mm)	4.01	N/A	3.62	3.36	3.08	1.61	2.92
LCA diameter (mm)	2.54	3.14	3.18	2.20	3.72	1.84	3.64
LSA diameter (mm)	3.62	3.10	3.22	2.41	2.46	2.97	2.83
Angle between DAA (°)	122.1	111.4	120.2	123.0	116.8	97.9	117.8
Angle between AA and RAA (°)	39.7	37.8	29.8	27.2	38.7	33.6	41.2
Angle between AA and LAA (°)	38.8	54.9	31.3	53.0	28.7	56.7	39.6
Clinical diagnosis	PFO	PFO, Trachea-stenosis	Trachea-stenosis	Trachea-stenosis	PFO	ASD, trachea-stenosis, pulmonary infection	VSD, MR, PAH

2 PFO, patent foramen ovale; VSD, ventricular septal defect; MR, mitral regurgitation; PAH, pulmonary arterial

3 hypertension; ASD, atrial septal defect.

4

5

Table 2 Summary of diameter and FDR of RAA and LAA

Case	1	2	3	4	5	6	7
LAA diameter (mm)	7.24	6.24	6.12	5.10	5.87	3.09	6.60
RAA diameter (mm)	7.37	6.57	8.18	7.73	6.17	6.80	5.03
FDR of LAA (LCA and LSA) (%)	20.38	29.21	21.89	15.81	28.66	20.74	28.99
FDR of RAA (RCA and RSA) (%)	34.65	17.85	36.64	35.21	24.72	24.56	26.88

Computational fluid dynamics investigation on aortic hemodynamics in double aortic arch before and after ligation surgery

Yunfei Ling^{a,b}, Torsten Schenkel^c, Jiguo Tang^{b*}, Hongtao Liu^b

^aDepartment of Cardiovascular Surgery, West China Hospital, Sichuan University, Chengdu 610041, China

^bState Key Laboratory of Hydraulics and Mountain River Engineering, College of Water Resource & Hydropower, Sichuan University, Chengdu 610065, China

^cDepartment of Engineering and Mathematics, Sheffield Hallam University, Sheffield S1 1WB, United Kingdom

Abstract: Double aortic arch (DAA) malformation is one of the reasons for symptomatic vascular rings, the hemodynamics of which is still poorly understood. Double aortic arch is the most common type of vascular ring often requiring surgical repair in childhood. The hemodynamics for the DAA remains unclear. This study aims to investigate the blood flow characteristics in patient-specific double aortic arches using computational fluid dynamics (CFD). Seven cases of infantile patients with DAA were collected and their computed tomography images were used to reconstruct 3D computational models. A modified Carreau model was used to consider the non-Newtonian effect of blood and a three-element Windkessel model taking the effect of the age of patients into account was applied to reproduce physiological pressure waveforms. Numerical results show that blood flow distribution and energy loss of DAA depends on relative sizes of the two aortic arches and their angles with the ascending aorta. Ligation of either aortic arch increases the energy loss of blood in the DAA, leading to the increase in cardiac workload. Generally, the rising rate of energy loss before and after the surgery is almost linear with the area ratio between the aortic arch without ligation and the ascending aorta.

Keyword: Double aortic arch; Non-Newtonian fluids; Three-element Windkessel model, Flow distribution; Energy loss

*Corresponding author.
E-mail address: tangjiguo@scu.edu.cn/tangjiguo@sina.cn (J. Tang)

1. Introduction

Double aortic arch (DAA) malformation is the most common cause of symptomatic vascular rings, arising from the persistence of the fourth aortic arches during embryonic development. In general, both left and right arches give rise to ipsilateral separate carotid and subclavian arteries (Hanneman et al., 2017). However, most DAA patients have one arch that is larger in size and extends higher cranially, categorizing the anomaly into dominant right arch (55-70%), dominant left arch (20-35%) and balanced arches (5-10%) (Temur et al., 2021). Symptoms of DAA include wheeze, dyspnea, recurrent pulmonary infection and dysphagia due to tracheal and esophageal compression.

Early surgical repair is recommended for all DAA patients to prevent aggravation of symptoms or even death. In practice, ligating the non-dominant arch with concurrent repair of other anomalies is usually performed on patients with one dominant arch (Alsenaidi et al., 2006; Yang et al., 2019). However, surgeries on balanced arches remain controversial since both arches are similar in diameter and the choice of intervened arch is based predominantly upon surgeons' experience. Subjective judgment may be insufficient considering the complex nature and multiple variations of aortic morphology as well as hemodynamics (Kaldararova et al., 2017), and suboptimal choice of ligated arch may lead to compromised prognosis, including insufficient neurological blood supply and decreased motor function of upper extremities.

Computational fluid dynamics (CFD) can be used to analyze hemodynamics even in complex anatomies (Taylor and Figueroa, 2009; Numata et al. 2016; Zhu et al., 2019; Ling et al., 2021), and has been reported providing highly resolved blood flow metrics for surgeons to base their treatments upon (Pirola et al., 2017; Singh et al., 2016). Although the aortic ligation and aneurysms of patient with single aortic arch were investigated by many researchers, little work on the hemodynamics of DAA with CFD method is published (Miyazaki et al., 2017; Hohri et al., 2021). Furthermore, the above studies are limited to single patients with DAA. In this study, we collected 7

cases of infantile patients with DAA. We performed the numerical simulations with their computed tomography (CT) imaged to investigate the aortic hemodynamics in DAA with different anatomical features. The aim of the present study was to elucidate the aortic hemodynamics in double aortic arch and the changes of flow distribution ratio and energy loss before and after ligating one of aortic arches to provide some references for the surgery.

2. Computational modeling and numerical method

In the present study, the flow is considered to be transient, three-dimensional, and laminar since the mean Reynolds number is less than 1000. The blood is regarded as an incompressible, non-Newtonian fluid with a density of 1060 kg/m³ (Boumpouli et al., 2021). Thus, the conservation equations can be described as:

$$\nabla \cdot \mathbf{v} = 0 \quad (1)$$

$$\rho \frac{\partial \mathbf{v}}{\partial t} + \mathbf{v} \cdot \nabla (\rho \mathbf{v}) = -\nabla P + \nabla \cdot (\mu \nabla \mathbf{v}) \quad (2)$$

where ρ is the blood density, v and P are the blood velocity and pressure. μ is the viscosity and is calculated using a modified Carreau model (Gambaruto et al., 2011; Pereira et al., 2013):

$$\mu = \mu_{\infty} + (\mu_0 - \mu_{\infty}) (1 + (\lambda \dot{\gamma})^2)^{\frac{n-1}{2}} \quad (3)$$

where the zero and infinite strain rate limit viscosities μ_0 and μ_{∞} are equal to 45.6 and 3.2 mPa s, respectively, the relaxation time constant λ is given by 10.03 s and the power law index n is 0.344.

Using constant or scaled inflow boundary conditions often arises in cardiovascular CFD. Effect of the two types of inlet flow rate on the simulation is presented in **Appendix A**. It is found that using constant or scaled inlet flow rate affects the values of WSS and energy loss, but has no obvious effect on the flow distribution ratio of each outlet and the variation trend of energy ratio before and after the surgery. In the present study, the scaled inflow boundary condition is applied. A pulsatile blood flow velocity waveform of ascending aorta (Fig. 1A) obtained by Kocaoglu et al. (2021) is used to reconstruct the inlet flow waves that are not available for the present patients.

75 Considering the difference with different patients, the flow waveform is interpolated to the heart
 76 rate and the average flow rate of each patient. Here, the flow rate is estimated using the weight of
 77 patients, $\bar{Q} = \text{weight} \times 120 \text{ mL/min}$. The heart rate, weight and other patients' information are
 78 given in Table 1. The BSA (body surface area) is estimated based on the references of DuBois and
 79 DuBois (1916) and Wang et al. (1992). Previous works showed that a rigid-wall assumption had no
 80 obvious effect on the resultant flow and stress fields (Pereira et al., 2013; Miyazaki et al., 2017),
 81 thus the arterial wall is assumed to be rigid. A three-element Windkessel model (WK3), as shown in
 82 Fig. 1B, is implemented at each outlet to reproduce physiological pressure P waveforms
 83 (Alimohammadi et al., 2014; Bonfanti et al., 2019):

$$84 \quad P = (R_1 + R_2)Q - R_2C \frac{dp}{dt} + R_1R_2C \frac{dQ}{dt} \quad (4)$$

85 where Q is flow rate, R_1 and R_2 are proximal and distal resistances, and C is the compliance of the
 86 vasculature distal to outlet. The derivative terms can be approximated using the forward Euler
 87 method for cases with small time step Δt :

$$88 \quad P_n = \frac{(R_1 + R_2 + R_1\beta)Q_n - R_1\beta Q_{n-1} + \beta P_{n-1}}{1 + \beta} \quad (5)$$

89 where $\beta = R_2C/\Delta t$. In the present study, we cannot obtain the accurate WK3 model parameters since it
 90 is difficult to measure the patient-specific inlet flow rate and pressure of each outlet for the very
 91 young patients. Therefore, these parameters are determined using the method similar to that used by
 92 Alimohammadi et al. (2014), Qiao et al. (2019) and Liao et al. (2021). Different from these
 93 previous works, the age has a significant effect on the WK3 parameters since the patients are very
 94 young (2-36 months old) in our study. Thus, we consider the effect of age in the following processes
 95 calculating the WK3 parameters. Firstly, the total resistance and the compliance at the i th outlet are
 96 estimated using:

$$97 \quad \bar{P}_i = R_{t,i} \bar{Q}_i \quad (6)$$

$$C_i = \frac{\tau}{R_{t,i}} \quad (7)$$

where the average flow rate \bar{Q}_i is calculated from the 0 Pa boundary condition simulations, the time constant τ is 1.79 s (Simon et al., 1979) and the average outlet pressure \bar{P}_i is estimated based on the standard formula $\bar{P}_i = P_{min} + 1/3(P_{max} - P_{min})$ (Alimohammadi et al., 2014). Since the patients are too young to measure their blood pressure waveform of each outlet, diastolic and systolic blood pressures are utilized to estimate the average outlet pressure of each outlet (Qiao et al., 2020). Then, the proximal resistance R_1 and distal resistance R_2 are calculated using:

$$R_{1,i} = \rho \cdot PWV / A_i \quad (8)$$

$$R_{2,i} = R_{t,i} - R_{1,i} \quad (9)$$

where A_i is the area of the i th outlet, and the pulse wave velocity PWV is related to the patient age and is calculated using the correlation proposed by Jarvis et al. (2020), $PWV=1.3+1.2M$, M is the age of the patient in month. In the present simulations, the coronary artery flow is not considered because the measured inlet flow data is lacked and the consideration of coronary arteries makes the three-element Windkessel model more complex. We thus use the ascending aorta without the coronary arteries as the simulated geometry to reduce the influence of excluding coronary arteries.

The simulations are performed using Ansys Fluent, and user defined functions (UDF) are applied to achieve the modified Carreau viscosity model and the three-element Windkessel model. A velocity table is read into Fluent to achieve the pulsatile velocity of the inlet. A double-precision pressure-based solver is employed. The PISO algorithm is used as the pressure-velocity coupling method. The second-order upwind scheme is adopted for the discretization of the governing equations. The least squared cell- based gradient evaluation method is applied to compute the gradient of the scalar. The standard scheme is used for the pressure interpolation. The time step is set to 0.001 s and the data from the 6th cardiac cycle are used to avoid the start-up effects and to achieve stable results (Cheng et al., 2014; Qiao et al., 2019).

122 The CT images of 7 infantile patients with double aortic arch were collected retrospectively and
 123 used to reconstruct the 3D computational model, as shown in Fig. 1C. The study was approved by
 124 the Ethics Committee of West China Hospital, Sichuan University, Chengdu, China (Ref No. 2022-
 125 26). In addition, written informed consent was obtained from all the guardian on behalf of the child
 126 participant. The diameters of ascending aorta (AA), descending aorta (DA), right carotid artery
 127 (RCA), right subclavian artery (RSA), left carotid artery (LCA), left subclavian artery (LSA) are
 128 summarized in Table 1.

129 The inlet is extruded for over 10 times in their radius to ensure the full development of ejected
 130 flow. The polygonal mesh with 12 prism layers at the walls (growth rate of 1.05) is generated and
 131 used in this work. Numerical simulations for case 1 with meshes of 0.69, 0.91 and 1.10 million cells
 132 are performed to test the mesh independence. The corresponding maximum wall shear stress (WSS)
 133 is 23.251, 23.351 and 23.354 Pa, respectively, resulting in a Grid Convergence Index (GCI) of
 134 0.002% (Celik et al., 2008). Thus, the mesh-generated method for the case with 1.10 million
 135 elements is used for all simulations. All simulations are performed on a server with two 64-core
 136 AMD EPCY-7702 CPUs and 256 G RAM. For each simulation, 60 cores are used and the
 137 computational time is about 30-50 minutes for 100 time steps. The total computational time is about
 138 11-33 hours for the cases with different cardiac cycles.

139 Table 1 Summary of patients' information, sizes of each inlet and outlet and clinical diagnosis

Case	1	2	3	4	5	6	7
Age (months)	9	2	3	11	11	36	36
Sex	Female	Female	Male	Female	Female	Male	Male
Heart rate (bpm)	132	136	160	109	130	162	97
Weight (kg)	9	6	6.8	10.7	8	6	11
Height (cm)	67	60	58	77	72	80	93
Body surface area (m ²)	0.39	0.30	0.31	0.46	0.386	0.37	0.53
AA diameter (mm)	10.14	9.37	9.64	9.25	8.48	7.46	9.21
DA diameter	1.43	5.70	5.37	5.48	6.81	4.85	6.35

(mm)							
RCA diameter	3.18	3.43	3.24	2.84	2.54	2.01	2.89
(mm)							
RSA diameter	4.01	N/A	3.62	3.36	3.08	1.61	2.92
(mm)							
LCA diameter	2.54	3.14	3.18	2.20	3.72	1.84	3.64
(mm)							
LSA diameter	3.62	3.10	3.22	2.41	2.46	2.97	2.83
(mm)							
Angle between	122.1	111.4	120.2	123.0	116.8	97.9	117.8
DAA (°)							
Angle between	39.7	37.8	29.8	27.2	38.7	33.6	41.2
AA and RAA (°)							
Angle between	38.8	54.9	31.3	53.0	28.7	56.7	39.6
AA and LAA (°)							
Clinical	PFO	PFO,	Trachea-	Trachea-	PFO	ASD,	VSD, MR,
diagnosis		Trachea-	stenosis	stenosis		trachea-	PAH
		stenosis				stenosis,	
						pulmonary	
						infection	

140 PFO, patent foramen ovale; VSD, ventricular septal defect; MR, mitral regurgitation; PAH, pulmonary arterial
141 hypertension; ASD, atrial septal defect.

142
143 In the present study, flow distribution ratio (FDR), energy loss (EL), spatial averaged WSS
144 (SAWSS) and time averaged WSS (TAWSS) are calculated and analyzed. The FDR is defined as
145 the flow rate ratio of each carotid artery and subclavian artery to ascending aorta:

$$146 \quad FDR = \frac{Q_{out,i}}{Q_{in}} \times 100\% \quad (10)$$

147 EL is calculated by the drops of static pressure and dynamic pressure between the inlet and the
148 outlets:

$$149 \quad EL = (P_{in} + \frac{1}{2} \rho \bar{u}_{in}^2) Q_{in} - \sum_{outlet} (P_{out} + \frac{1}{2} \rho \bar{u}_{out}^2) Q_{out} \quad (11)$$

150 where \bar{u}^2 is the average blood velocity.

151 SAWSS and TAWSS are obtained by averaging the WSS on the wall of the whole vessel at
152 different time and the local WSS through a cardiac cycle, respectively, and can be expressed as:

153
$$SAWSS = \frac{1}{S} \int_S |\tau(s, t)| ds \quad (12)$$

154
$$TAWSS = \frac{1}{T} \int_0^T |\tau(s, t)| dt \quad (13)$$

155 where S and T are the area of surface wall and the cardiac period.

156 **3. Results and discussion**

157 **3.1. Hemodynamics of DAA before and after removing aortic arch**

158 For the patient with DAA, it is necessary to determine which aortic arch should be ligated
159 before the surgery. However, this is very difficult due to the complex hemodynamics of DAA,
160 especially for the patient with balanced arches (Hohri et al., 2021). To better guide the surgeries,
161 here we discuss the hemodynamics of DAA before and after ligating right aortic arch (RAA) and
162 left aortic arch (LAA) using a typical balanced geometry model (case 1). Fig. 2 shows the
163 distribution of averaged wall pressure and the blood flow velocity streamlines during peak systole
164 before and after the surgery. The wall pressure of the arteries gradually decreases from ascending
165 aorta to descending aorta along the blood flow direction. The high-pressure region occurs at the
166 bifurcation of the two aortic arches due to the collision of blood upon the vessel wall directly, which
167 will not be observed in single aortic arch. Ligating either aortic arch has no obvious effect on the
168 maximum wall pressure of the arteries, as shown in Fig. 2. The wall pressure distribution is not
169 changed obviously after the ligation of LAA or RAA. As for the streamlines, velocity magnitude is
170 high in the RCA, RSA, LCA and LSA, as expected. After the ligation of one aortic arch, the
171 maximum velocity increases obviously, and the streamlines get more helical in the carotid and
172 subclavian arteries in the ligated side of ascending aorta.

173 Fig. 3 shows the variations of blood flow rate and pressure at each outlet during a cardiac cycle

for case 1. The results of other cases are provided in **Appendix B**. The time-averaged flow rates from each outlet are summarized in **Appendix C**. The outlet blood flow and pressure show a similar trend before and after the ligation either aortic arch. Over 44% of blood outflows through the descending aorta in the original DAA case, and this ratio decreases after the surgery slightly. The flow rate peak of RCA, RSA, LCA and LSA occurs earlier than the inlet flow peak, but that of descending aorta is slightly later than the inlet flow peak. The pressure of descending aorta is reduced when one of aortic arches is ligated, but that of RCA, RSA, LCA and LSA is increased after the surgery.

The variation of SAWSS and the distribution of TAWSS are shown in Fig. 4. Although the temporal variation of SAWSS exhibits a similar shape, its maximum is increased after ligating one of the aortic arches because of the increase in flow rate in the remaining untreated aortic arch. It is worth noting that TAWSS is elevated considerably in the bifurcation between two aortic arches after ligating RAA owing to the larger angle between AA and LAA than that between AA and RAA. When the RAA is ligated, more blood flows through the LAA with an obvious change in flow direction, leading to a high-velocity gradient region.

Fig. 5 shows the energy loss for DAA in case 1 without surgery, ligating LAA or RAA. Similar to the results of an adult single aortic arch (Qiao et al., 2019), the EL for DAA reaches its maximum ($t/T=0.18$) before peak systole ($t/T=0.23$). After the ligation of either aortic arch, the EL reaches the maximum at $t/T=0.114$. The time averaged EL is 6.1 mW before the surgery, while it increases to 9.5 mW (+55%) and 8.5 mW (+39%) after the ligation of LAA and RAA, respectively. This indicates that ligating one of the aortic arches for the patient with DAA will increase the cardiac workload. Although the diameters of LAA and RAA are very similar in case 1, the difference of EL after the removal of LAA and RAA can reach 1 mW, or 16% higher EL for the unfavorable variant. It has to be noted that case 1 is the case that shows the smallest changes before/after and between left and right AA ligations, other cases show more dramatic differences.

3.2. Effect of anatomical features on operative effect

Fig. 6 shows the effect of anatomical features on the blood flow distribution from each outlet and the ratio of blood flow going to brain (LCA and RCA) and to systemic vessels (LSA, RSA and DA) before and after the surgery. Table 2 summarizes the diameter of RAA and LAA, and the FDR of LAA (LCA and LSA) and RAA (RCA and RSA). About 20%-40% blood outflows through LCA and RCA to the brain of patients, as shown in Fig. 6B. For the size-balanced DAA case 5, the FDR of RAA and LAA is similar. However, for the size-balanced DAA cases 1 and 2, the FDR of RAA and LAA differs from each other obviously, similar to the results of an adult patient with DAA reported by Hohri et al. (2021). For the unbalanced DAA cases 3 and 4, the larger aortic arch has higher flow rate, but the FDR of RAA and LAA is not different considerably for the cases 6 and 7, as shown in Fig. 6A. It is more reasonable for determining the dominant arch using the blood flow rate from the left and right carotid and subclavian arteries rather than the diameter of RAA and LAA based on the study of Hohri et al. (2021). Thus, determining the dominant arch of DAA with the CFD method may be more valid than that only with the CT images owing to the considerable effect of various anatomical features.

Table 2 Summary of diameter and FDR of RAA and LAA

Case	1	2	3	4	5	6	7
LAA diameter (mm)	7.24	6.24	6.12	5.10	5.87	3.09	6.60
RAA diameter (mm)	7.37	6.57	8.18	7.73	6.17	6.80	5.03
FDR of LAA (LCA and LSA) (%)	20.38	29.21	21.89	15.81	28.66	20.74	28.99
FDR of RAA (RCA and RSA) (%)	34.65	17.85	36.64	35.21	24.72	24.56	26.88

It is noted that, for the size-balanced cases 1, 2 and 5 and the slightly unbalanced cases 3 and 7 (area ratio of arches less than 2), there is no obvious change in the blood flow distribution before and after either aortic arch. However, for the severely unbalanced cases 4 and 6 (area ratio of arches larger than 2), the blood flowing out from the descending aorta is disturbed after the ligation of RAA (larger arch) obviously, leading to the decrease in the FDR of DA. However, this effect is not

noticeable after ligating the LAA (smaller arch). This is due to that the blood out from descending aorta has to flow through an aortic arch with larger flow resistance after the surgery, resulting in the reduction of FDR of descending aorta. The above simulation results implicate that arch area ratio of 2 may be the critical value determining whether the smaller arch must be the ligated one in the surgery.

The energy loss throughout a cardiac cycle for different patients before and after surgeries is shown in Fig. 7. It can be seen that the energy loss for case 6 is considerably larger than other cases due to the poorly developed aortic arch. After ligating either aortic arch, the energy loss will increase slightly for most cases, as shown in Fig. 7A. While in size-balanced cases (case 1) we observe only minor differences (16%) between RAA and LAA ligation, in unbalanced cases this difference can be as high as 264% (Case 6, LAA vs RAA ligation). This total energy loss is concurrent with a drop in descending aorta FDR. Our results show that in all the cases studied the blood supply to the subclavian and carotid arteries is unimpeded or slightly increased in most cases, and increased even in the critical cases (Case 6, RAA ligation), while support to the lower body is most directly affected negatively in the critical cases. In order to support surgeons in their decision making, we propose two geometric parameters to show the effect of anatomical features of DAA on the energy loss after the surgery. The first one is the area ratio of the ascending aorta to the aortic arch without ligation A_0/A_{rem} . The other one is the angle between the normal direction of ascending aorta and the aortic arch without ligation θ_{rem} , as shown in Fig. 7B. Figure 7 C and D shows the dependency of EL on the area ratio A_0/A_{rem} in panel C and on the angle θ_{rem} in panel D. The dependency of the respective other parameter – angle in panel C, and area ratio in panel D – is shown in the marker size. A statistical analysis of the data is also performed and the results are given in **Appendix D**. The coefficient of determination R^2 that is a statistical measure in a regression model is used to describe the independent of energy loss ratio on different variables. It is interesting that the energy loss ratio before and after the surgery depends on the A_0/A_{rem} ($R^2=0.805$)

whichever aortic arch is ligated, as shown in Fig. 7 C. While in the current sample the largest EL increases were seen for RAA ligations – consistent with the higher occurrence of RAA dominant cases – the correlation between EL increase and area ratio is clear and linear in Fig. 7 C. Although both EL_{before} and EL_{after} are affected by the θ_{rem} due to the change of flow direction in the DAA, the correlation between EL ratio and θ_{rem} is less clear ($R^2=0.424$) in Fig. 7 D. While there is a correlation between angle and EL there are more outliers in this graph. It is interesting, though, that these outliers are all RAA dominant cases, where the RAA ligation leads to a relatively low EL for a high angle case (case 2) and to relatively low EL for low angle cases (cases 3 and 5). Thus, based on the simulation results, the variation of FDR and energy loss after the surgery of DAA can be estimated by A_R/A_L , θ_R/θ_L and A_0/A_{rem} roughly to help to optimize the surgical planning.

3.3. Limitations

In this study, we perform simulations with a series of patient-specific geometries reconstructed from CT images taking the Non-Newtonian effect into account. However, the inlet and outlet conditions are still unsure since the patients are too young (2-36 months old) to measure their blood flow velocity in the present study. To overcome this issue, an inlet velocity waveform measured by Kocaoglu et al. (2021) not the patient-specific one is used and reconstructed based on the patient-specific heart rate and the average flow rate estimated using the weight of patients, and the three-element Windkessel model is applied to reproduce physiological pressure waveforms of each outlet. In addition to this, similar to most of previous studies, the vessel wall is assumed to be rigid and a flat velocity profile is given to the extruded boundary. Some previous works showed that the above assumptions have no obvious effect on blood flow ratio and the distal blood flow of the aortic arch but affect the value of WSS (Miyazaki et al., 2017; Boumpouli et al., 2021).

4. Conclusions

The present study investigated the patient-specific blood flow in the double aortic arch (DAA) before and after surgery with the CFD method. We collected seven cases of infantile patients with

271 DAA and used their computed tomography images to reconstruct 3D computational models. A
272 three-element Windkessel model taking the effect of patient age into account was applied to
273 reproduce physiological pressure waveforms in the simulations. Results show that the anatomical
274 features and surgery program have a considerable effect on the WSS, flow distribution ratio and
275 energy loss for DAA. After ligating one of the aortic arches, the blood flow from the descending
276 aorta is generally reduced when the area ratio of the arch area ratio is larger than 2. The energy loss
277 ratio before and after ligating one aortic arch is proportional to the area ratio of the remained aortic
278 arch in surgery to the ascending aorta. Overall, the present study indicates that the CFD analysis can
279 contribute to a further understanding of hemodynamics in DAA and provide some references for the
280 surgery.

281 **CRedit authorship contribution statement**

282 **Yunfei Ling:** Conceptualization, Investigation, Writing - original draft, Funding acquisition.
283 **Torsten Schenkel:** Formal analysis, Data Curation, Writing - original draft, Writing - review &
284 editing, Visualization. **Jiguo Tang:** Conceptualization, Supervision, Methodology, Writing - original
285 draft, Writing - review & editing, Project administration, Funding acquisition. **Hongtao Liu:**
286 Validation, Software, Formal analysis.

287 **Declaration of Competing Interest**

288 The authors declare that they have no known competing financial interests or personal
289 relationships that could have appeared to influence the work reported in this paper.

290 **Acknowledgements**

291 The authors are profoundly grateful to the financial supports of the Sichuan Science and
292 Technology Program (Grant No. 2021YJ0374) and the 1·3·5 project for disciplines of excellence-
293 Clinical Research Incubation Project, West China Hospital, Sichuan University (ZYJC21064).

294 **References**

295 Alsenaidi, K., Gurofsky, R., Karamlou, T., Williams, W.G., McCrindle, B.W., 2006. Management

296 and outcomes of double aortic arch in 81 patients. *Pediatrics* 118, 1336-1341.

297 Alimohammadi, M., Agu, O., Balabani, S., Díaz-Zuccarini, V., 2014. Development of a patient-
 298 specific simulation tool to analyse aortic ligations: Assessment of mixed patient-specific flow
 299 and pressure boundary conditions. *Med. Eng. Phy.* 36, 275-284.

300 Bonfanti, M., Franzetti, G., Maritati, G., Homer-Vanniasinkam, S., Balabani, S., Díaz-Zuccarini, V.,
 301 2019. Patient-specific haemodynamic simulations of complex aortic ligations informed by
 302 commonly available clinical datasets. *Med. Eng. Phys.* 71, 45-55.

303 Boumpouli, M., Sauvage, E.L., Capelli, C., Schievano, S., Kazakidi, A., 2021. Characterization of
 304 flow dynamics in the pulmonary bifurcation of patients with repaired tetralogy of fallot: A
 305 computational approach. *Front. Cardiovasc. Med.* 8, 703717.

306 Celik, I., Ghia, U., Roache, P. J., Freitas, C. J., Coleman, H., Raad, P. E., 2008. Procedure for
 307 estimation and reporting of uncertainty due to discretization in CFD applications. *J. Fluid. Eng.*,
 308 130, 078001.

309 Cheng, Z., Juli, C., Wood, N. B., Gibbs, R. G. J., Xu, X. Y., 2014. Predicting flow in aortic ligation:
 310 comparison of computational model with PC-MRI velocity measurements. *Medical Engineering*
 311 *and Physics* 36, 1176-1184.

312 DuBois D., DuBois E.F., 1916. A formula to estimate the approximate surface area if height and
 313 weight be known. *Arch. Intern. Medicine* 17 863-71.

314 Gambaruto, A.M., Janela, J., Moura, A., Sequeira, A., 2011. Sensitivity of hemodynamics in a
 315 patient specific cerebral aneurysm to vascular geometry and blood rheology. *Math. Biosci. Eng.*
 316 8, 409–423.

317 Hanneman, K., Newman, B., Chan, F., 2017. Congenital Variants and Anomalies of the Aortic Arch.
 318 *Radiographics* 37, 32-51.

319 Hohri, Y., Numata, S., Itatani, K., Inoue, T., Yaku, H., 2021. Determination of the dominant arch by
 320 computational fluid dynamics analysis using computed tomography images in double aortic

321 arch. *Int. J. Cardiovasc. Imaging* 37, 2573-2575.

322 Jarvis K., Soulat G., Scott M., Vali A., Pathrose A., Syed A.A., Kinno M., Prabhakaran S., Collins
323 J.D., Markl M., Investigation of aortic wall thickness, stiffness and flow reversal in patients with
324 cryptogenic stroke: a 4D flow MRI study, *J. Magn. Reson. Imag.* 53, 942-952.

325 Kaldararova, M., Simkova, I., Varga, I., Tittel, P., Kardos, M., Ondriska, M., Vrsanska, V., Masura,
326 J., 2017. Double aortic arch anomalies in Children: A Systematic 20-Year Single Center Study.
327 *Clin. Anat.* 30, 929-939.

328 Kocaoglu, M., Pednekar, A., Tkach, J. A., Taylor, M.D., 2021. Quantitative assessment of velocity
329 and flow using compressed SENSE in children and young adults with adequate acquired
330 temporal resolution. *J. Cardiovasc. Magn. Reson.* 23, 113.

331 Liao, Z.J., Qin, S.L., Chen, R.L., Cai, X.C., 2021. A parallel domain decomposition method for
332 large eddy simulation of blood flow in human artery with resistive boundary condition. *Comput.*
333 *Fluids* 232, 105201.

334 Ling, Y.F., Tang, J.G., Liu, H., 2021. Numerical investigation of two-phase non-Newtonian blood
335 flow in bifurcate pulmonary arteries with a flow resistant using Eulerian multiphase model.
336 *Chem. Eng. Sci.*, 233, 116426.

337 Miyazaki, S., Itatani, K., Furusawa, T., Nishino, T., Sugiyama, M., Takehara, Y., Yasukochi, S,
338 2017. Validation of numerical simulation methods in aortic arch using 4D Flow MRI. *Heart*
339 *Vessels* 32, 1032-1044.

340 Numata, S., Itatani, K., Kanda, K., Doi, K., Yamazaki, S., Morimoto, K., Manabe K., Ikemoto, K.,
341 Yaku, H., 2016. Blood flow analysis of the aortic arch using computational fluid dynamics.
342 *European Journal of Cardio-Thoracic Surgery*, 49, 1578-1585.

343 Pereira, J. M. C., Serra e Moura, J. P., Ervilha, A. R., Pereira, J. C. F., 2013. On the uncertainty
344 quantification of blood flow viscosity models. *Chem. Eng. Sci.* 101, 253-265.

345 Pirola, S., Cheng, Z., Jarral, O.A., O'Regan, D.P., Pepper, J.R., Athanasiou, T., Xu, X.Y., 2017. On

the choice of outlet boundary conditions for patient-specific analysis of aortic flow using computational fluid dynamics. *J. Biomech.* 60, 15-21.

Qiao, Y., Fan, J., Ding, Y., Luo, K., Zhu, T., 2019. A primary computational fluid dynamics study of pre-and post-TEVAR with intentional left subclavian artery coverage in a type B aortic ligation. *J. Biomech. Eng.* 141, 111002.

Qiao, Y., Mao, L., Ding, Y., Fan, J., Zhu, T., Luo, K., 2020. Hemodynamic consequences of TEVAR with in situ double fenestrations of left carotid artery and left subclavian artery. *Med. Eng. Phy.* 76, 32-39.

Simon, A.C., Safar, M., Levenson, J., London, G., Levy, B., Chau, N., 1979. An evaluation of large arteries compliance in man. *Am. J. Physiol.-Heart C.* 237, H550-H554.

Singh, S.D., Xu, X.Y., Wood, N.B., Pepper, J.R., Izgi, C., Treasure, T., Mohiaddin, R.H., 2016. Aortic flow patterns before and after personalised external aortic root support implantation in Marfan patients. *J. Biomech.* 49, 100-111.

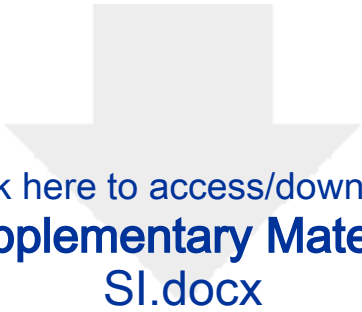
Taylor, C. A., Figueroa, C. A., 2009. Patient-specific modeling of cardiovascular mechanics. *Annual Review of Biomedical Engineering*, 11, 109-134.

Temur, H.O., Yozgat, C.Y., Uzuner, S., Ugurlucan, M., Yazan, H., Cakir, E., Yozgat, Y., 2021. Balanced Double Aortic Arch Causing Persistent Respiratory Symptoms Mimicking Asthma in an Infant. *J. Pediatr. Intensive. Care* 10, 162-166.

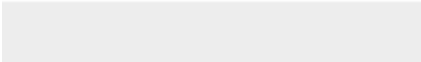

Wang Y., Moss J., Thisted R., 1992. Predictors of body surface area. *J. Clin. Anesth.* 4, 4-10.

Yang, Y., Jin, X., Pan, Z., Li, Y., Wu, C., 2019. Diagnosis and surgical repair of congenital double aortic arch in infants. *J. Cardiothorac. Surg.* 14, 160.

Zhu, Y., Zhan, W., Hamady, M., Xu, X.Y., 2019. A pilot study of aortic hemodynamics before and after thoracic endovascular repair with a double-branched endograft. *Medicine in Novel Technology and Devices* 4, 100027.



Click here to access/download
Supplementary Material
SI.docx



Conflict of Interest Statement:

The authors declare that they have no known competing financial interests or personal relationships that could have appeared to influence the work reported in this paper.